

Design and Control of a Fully Actuated Aerial Manipulator System for Measuring the Thickness of Metal Facilities

Shuang Hao^{ID}, Member, IEEE, Juzheng Mao^{ID}, Graduate Student Member, IEEE, Junyi Zhang^{ID}, Xiangyang Zhao^{ID}, Guangming Song^{ID}, Senior Member, IEEE, Aiguo Song^{ID}, Senior Member, IEEE, and Peter Xiaoping Liu^{ID}, Fellow, IEEE

Abstract—An aerial manipulator (AM) system for thickness measurement of metal facilities is introduced in this article, which includes a fully actuated flying platform and an end effector. The AM utilizes the fully actuated advantage of the flying platform to apply controlled contact forces to the environment without the need for complex robotic manipulators. An end effector is designed, which includes an ultrasonic thickness (UT) probe mounted on a spring-damping buffer, and a coupling agent injection device allows the coupling to be applied during the inspection process. We divide the aerial inspection process into two phases: the approach phase and the contact phase. In the approach phase, we design a yaw control assistance method to ensure that the AM can contact the target surface with the desired yaw, even outside the operator's line of sight. In the contact phase, a parallel force/velocity controller tailored to the motion characteristic of the AM is proposed to achieve precise contact force control. A switching function is designed to ensure stable transitions between the motion control and force control. The control effectiveness and the ability to measure the thickness of the metal facility of the AM system are demonstrated by practical experiments.

Index Terms—Aerial contact inspection, aerial manipulator (AM), aerial physics interaction, force control, autonomous aerial vehicle (AAV).

I. INTRODUCTION

INDUSTRIAL facilities require regular inspections to ensure the safety of industrial production. Traditional manual inspections are time-consuming and labor intensive, and the inspection frequency increases with the age of the industrial facilities, leading to higher inspection costs. In some industrial inspection scenarios, such as high-altitude

Received 12 September 2024; revised 6 November 2024; accepted 12 November 2024. Date of publication 25 February 2025; date of current version 10 March 2025. This work was supported in part by the National Natural Science Foundation of China under Grant 62373098, Grant 61973076, Grant 52127813, and Grant 62103197; and in part by the Joint Fund Project under Grant 8091B042206. The Associate Editor coordinating the review process was Dr. Hongtian Chen. (*Corresponding author: Guangming Song.*)

Shuang Hao, Juzheng Mao, Junyi Zhang, Xiangyang Zhao, Guangming Song, and Aiguo Song are with the State Key Laboratory of Digital Medical Engineering, Jiangsu Key Laboratory of Remote Measurement and Control, School of Instrument Science and Engineering, Southeast University, Nanjing 210096, China (e-mail: shuanghao@seu.edu.cn; j.mao@ieee.org; zhangjy97@seu.edu.cn; Xiangyang_Zhao96@163.com; mikesong@seu.edu.cn; a.g.song@seu.edu.cn).

Peter Xiaoping Liu is with the Department of Systems and Computer Engineering, Carleton University, Ottawa, ON K1S 5B6, Canada (e-mail: xp.liu@sce.carleton.ca).

Digital Object Identifier 10.1109/TIM.2025.3545495

inspections, ensuring that the safety of inspection personnel is challenging. Driven by “Industry 4.0,” automated inspection is gradually becoming a key technology for enhancing the efficiency of industrial facility inspections and ensuring production safety [1].

In recent years, the autonomous aerial vehicle (AAV) technology has been widely used for inspection missions [2], [3], [4], [5], [6]. Compared with traditional manual inspections, the AAV is highly flexible, with high inspection efficiency and safety. Currently, AAV-based inspections primarily focus on noncontact methods, using cameras or LiDAR systems to inspect the surfaces of industrial facilities [7], [8]. For internal defects in industrial facilities, equipment such as ultrasonic/eddy current flaw detectors are usually used for contact inspection. Therefore, aerial manipulators (AMs) have attracted the attention of researchers which is an integrated system comprising a AAV and a robotic manipulator [9], designed to actively interact with the environment.

The AM was initially applied to tasks involving brief interaction with the environment, such as grasping [10], picking, and placing [11], [12]. In these tasks, the impact of interaction forces on the AM control is minimal or negligible. However, for contact inspection, the AM needs to be in contact with the target surface for a long time, making the interaction force an important factor affecting the stable control of the AM. Therefore, the interaction control between the AM and the environment has become a research hotspot in recent years [13], [14], [15]. A typical application scenario is shown in Fig. 1.

Traditional AAVs are underactuated systems, meaning that their position and attitude cannot be independently controlled. To achieve stable active interaction with the environment, they must be equipped with multidegree-of-freedom (DoF) manipulators [16]. This makes the system more complex, increases control difficulty, and raises costs. The fully actuated AAVs can achieve independent control of position and attitude which is suitable for aerial physical interaction control, i.e., fully actuated AAVs only need to be equipped with simple end effectors to interact stably with the environment. Therefore, in recent years, some scholars have conducted studies on aerial physical interaction based on fully actuated AMs [17], [18].

The aerial contact inspection using AMs can be divided into two phases: the approach phase and the contact phase

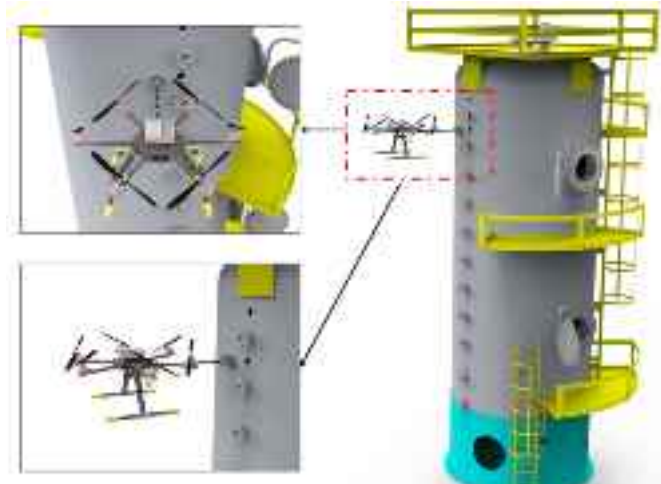


Fig. 1. Example scenario for the AM-based aerial contact inspection.

[19]. Due to limitations in robotic automation technology, AAV-based inspections are typically conducted with remote human control or supervision. For noncontact inspections, AAVs generally only need to hover at a certain distance from the target surface. For contact-based inspections, during the contact phase, the AM must approach the target surface slowly to reduce the impact during contact and ensure that the end-effector contacts the target surface in the desired attitude. As the AM approaches the target surface, the camera's field of view gradually decreases, making it difficult for the operator to control the AM's attitude relative to the target surface, especially the yaw angle, using 2-D images. When the AM end effector cannot contact the target surface with the desired attitude, it may result in the AM colliding with the target surface. Therefore, controlling the relative attitude of the AM to the target surface during the approach phase is a crucial issue for aerial contact inspection. In [20], a 2-D LiDAR is used to calculate the angle between the AM's flight direction and the target surface's normal direction. However, the weight of the 2-D LiDAR could negatively affect the AM's endurance. In [13] and [21], an RGB-D camera-based random sample consensus (RANSAC) method is used to determine the normal direction of the target surface, but the RGB-D camera is susceptible to outdoor lighting conditions. While 2-D LiDAR and RGB-D cameras can be used to obtain the yaw error of the AM, they require computational resources to ensure real-time performance. Therefore, an efficient yaw control assistance method is needed to make the AM contact the target surface with the desired attitude during the approach phase.

During the contact phase of aerial contact inspection, the AM end effector needs to maintain stable contact with the target surface. In some scenarios, the interaction force control is necessary, as excessive interaction force may damage contact sensors. At the same time, too little contact force may result in poor coupling between the sensor and the target surface. Therefore, the aerial interaction force control has become a recent research hotspot in the field of AM, with two main control methods: impedance/admittance control and force/motion hybrid control [19], [22], [23], [24]. The

impedance and admittance control are indirect methods of force control that generate interaction forces through positional differences by setting the desired trajectory points behind the target surface. This method requires prior knowledge of the precise geometric model of the environment and highly accurate self-positioning, which poses challenges, especially for suspended-base AMs. The force/motion hybrid control method divides the task space into complementary orthogonal subspaces, performing direct force control and motion control, respectively. However, this method may reduce robustness due to the switching process between motion control and force control [25]. In [17], [26], and [27], direct force control is combined with impedance control to achieve more stable force control. However, the impedance parameter selection and desired trajectory generation in the impedance control part remain challenging aspects for implementing this method in the AM control.

Based on the discussions above, this article presents a fully actuated AM system designed for thickness measurement of aerial metal facilities. The flying platform is a hexacopter with tilted rotors, allowing for decoupled control of both position and attitude. As a result, the AM does not require a multi-DoF manipulator to apply force. The end effector, connected to the flying platform via a rigid rod, includes an ultrasonic thickness (UT) probe, a spring-damping buffer, and a coupling agent injection device, enabling thickness measurements of metal structures.

During the approach phase, two laser range sensors mounted on the AM measure the distance to the target surface and calculate the yaw error, allowing the AM to adjust its yaw and prevent unsafe contact. Compared with the method based on an RGB-D camera Stephens et al. [13] and Fauli et al. [21], the proposed approach is less affected by lighting conditions. Unlike a 2-D LiDAR mounted on the flying platform [20], the laser range sensors are compact and lightweight. In addition, the proposed method calculates the AM's yaw error and performs yaw adjustment using only the measurements from the two laser rangefinders, which is computationally simple and requires minimal resources. In the contact phase, a parallel force/velocity controller is proposed, consisting of a velocity proportional-differential (PD) controller and a force proportional-integral (PI) controller. The velocity controller generates an initial interaction force, while the force PI controller compensates for force errors. The integral action of the force controller eliminates the steady-state error in contact force, with the velocity controller's output serving as a feedforward compensation. A switching function is also designed to control the force controller's activation, preventing undesired switching due to noise from the force sensor. Unlike traditional force/motion hybrid control, the proposed method applies the velocity controller throughout the entire process. During transitions between free flight and contact phases, only the output of the force PI controller switches, and the force PI controller mainly plays a compensatory role. Therefore, this approach reduces the chattering that might arise from switching between motion and force control.

The velocity controller remains active throughout the process, avoiding the frequent switching between force

and motion controllers typical of hybrid force/motion control.

The effectiveness of the proposed control method is validated through practical experiments. In addition, stepped-thickness steel plates are used to simulate metal structures, and the designed AM conducts thickness measurements. The results, analyzed and compared with manual measurements, demonstrate the application value of the proposed AM system for the thickness measurement of aerial metal structures.

The contributions of this article are as follows.

- 1) This article presents a fully actuated AM system, incorporating a fully actuated flying platform and a specialized end effector, specifically designed to enhance the efficiency of thickness measurements for high-altitude metal structures.
- 2) To achieve high efficiency and accuracy in aerial contact-based thickness measurements, this work introduces novel control strategies tailored for the AM's approach and contact phases, ensuring reliable data acquisition during inspection.
- 3) A comprehensive series of practical experiments is conducted to validate the effectiveness of the proposed AM system in measuring the thickness of metal facilities. The results include a detailed analysis of control performance and measurement accuracy, underscoring the system's potential for reliable and high-precision metal thickness measurements.

The remainder of this article is organized as follows. The design of the AM is shown in Section II. The system modeling and control of the AM are described in Section III. In Section IV, the developed interaction control system, comprising both approach and contact phase control, is presented. The experimental results are introduced in Section V. Finally, the conclusion and future work is summarized in Section VI.

II. AM SYSTEM OVERVIEW

To meet aerial inspection demands, the AM system is designed with strong contact stability, a simple maintenance-friendly structure, and sensor integration with the end effector. The proposed AM comprises a flying platform and an end effector, as shown in Fig. 2.

Unlike traditional under actuated flying platforms which thrust generated by their propellers is parallel, the fully actuated hexacopter in this study features tilted propellers. The tilting sacrifices some of the pulling force but enables the decoupling of position and attitude through the special control allocation design. This design allows for stable interaction with the environment without the need for a multi-Dof robotic manipulator, reducing both mechanical complexity and control difficulty.

The end effector includes a UT probe linked to a UT gauge, a spring-damping buffer for impact absorption, and a 1-D force sensor for measuring contact force. The coupling agent injection device, with an electric actuator, allows for remote control of the agent application. The UT gauge communicates with the host computer via wireless RS-485. Since the end effector is rigidly attached to the fully actuated hexacopter, its attitude aligns with that of the hexacopter. Therefore,

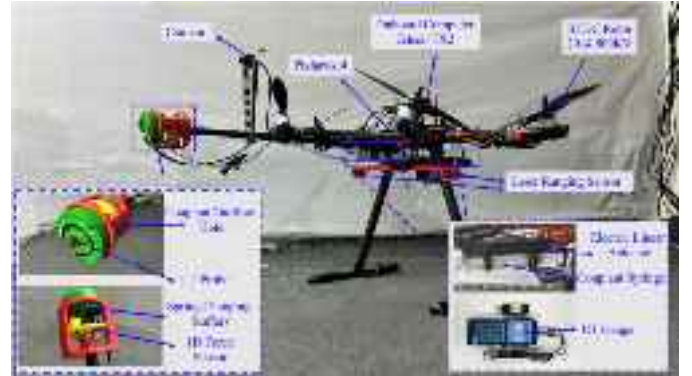


Fig. 2. Overview of the proposed AM system components.

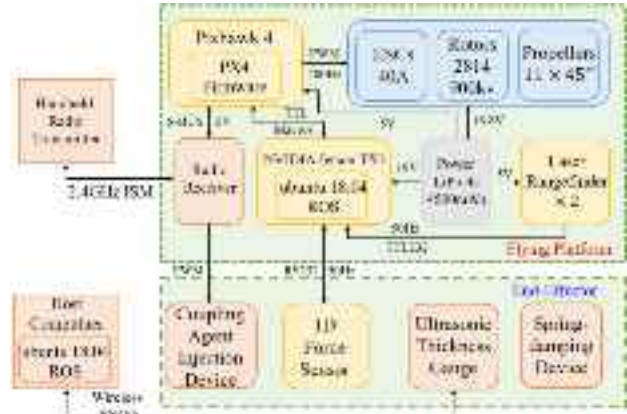


Fig. 3. Software and hardware frameworks of AM.

TABLE I
KEY SPECIFICATIONS AND PERFORMANCE INDICATORS
OF THE AM SYSTEM

Specification	Value
Total System Mass (Including Battery)	3.46 kg
Contact Device Mass	95 g
Maximum Contact Force	10 N
Maximum Payload Capacity	2 kg
Flight Duration	8 min
UT Gauge Accuracy	$0.5\%H + 0.05 \text{ mm}$ (H is the metal thickness)
UT Gauge Communication Range	50 m (Open Area)

controlling the flying platform directly enables control of the end effector. These components ensure efficient and stable aerial inspections.

The AM system's software and hardware framework are shown in Fig. 3. The flight controller, running on Pixhawk, receives force sensor and laser rangefinder data from the onboard computer via Mavros for control. Operators can use a radio transmitter to control both the flying platform and the coupling agent injector simultaneously, simplifying operation. The UT probe measures and sends thickness data to the host computer once it is properly coupled with the target surface. The main features of the AM are listed in Table I.

III. AM SYSTEM MODELING AND CONTROL

A. Modeling of AM

The coordinate frames of AM are marked in Fig. 2. The meaning of each coordinate frame is provided in Table II. The

TABLE II
DEFINITIONS OF THE COORDINATE FRAME
AND ROTATION MATRIX

Symbol	Definition
$\mathcal{F}_* : \{O_*, \mathbf{x}_*, \mathbf{y}_*, \mathbf{z}_*\}$	frame: origin and primary axes
W	world frame of the AM subscript
B	AM frame subscript
P	i -th rotor frame subscript
E	AM end-effector frame subscript
R_A^B	rotation matrix from \mathcal{F}_A to \mathcal{F}_B

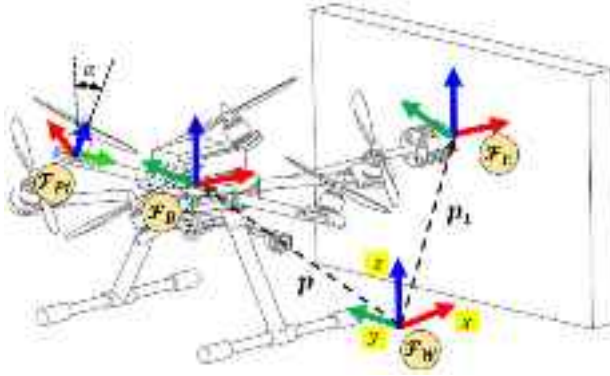


Fig. 4. Schematic of the important frames of AM.

center of mass (CoM) is designed to be at the geometric center of the hexacopter. We define $\mathbf{p} \in \mathbb{R}^3$ and $\mathbf{v} = [v_x, v_y, v_z]^T \in \mathbb{R}^3$ as the position and the velocity in \mathcal{F}_W . $\boldsymbol{\omega} \in \mathbb{R}^3$ is the angular velocity. $\Phi = [\phi, \theta, \psi]^T$ represents the roll-pitch-yaw Euler angle of the AM. The attitude of the AM is represented by a rotation matrix $\mathbf{R}_B^W \in \text{SO}(3)$.

The kinematic model of the fully actuated hexarotor is as follows:

$$\begin{cases} \dot{\mathbf{p}} = \mathbf{v} \\ \dot{\mathbf{R}}_B^W = \mathbf{R}_B^W [\boldsymbol{\omega}]_\times \end{cases} \quad (1)$$

where $[\cdot]_\times \in \text{so}(3)$ represents the skew-symmetric matrix of vector $\cdot \in \mathbb{R}^3$.

The end-effector position \mathbf{p}_t expressed in \mathcal{F}_W is given by

$$\mathbf{p}_t = \mathbf{p} + \mathbf{R}_B^W \mathbf{d} \quad (2)$$

where $\mathbf{d} \in \mathbb{R}^3$ represents the position of the tool-tip in \mathcal{F}_B which can be measured.

The dynamic model of the AM can be expressed as follows [19]:

$$\begin{cases} m\dot{\mathbf{v}} = m[0 \ 0 \ g]^T - \mathbf{R}_B^W \mathbf{F}_B + \mathbf{F}_e \\ \mathbf{J}\dot{\boldsymbol{\omega}} = \boldsymbol{\tau} - \boldsymbol{\omega} \times \mathbf{J}\boldsymbol{\omega} + \boldsymbol{\tau}_e \end{cases} \quad (3)$$

where $m \in \mathbb{R}$ and $\mathbf{J} = \text{diag}(J_{xx}, J_{yy}, J_{zz}) \in \mathbb{R}^{3 \times 3}$ represent the mass and inertia matrix of the AM, $\mathbf{F}_B \in \mathbb{R}^3$ and $\boldsymbol{\tau} \in \mathbb{R}^3$ represent the control force and torque with respect to \mathcal{F}_B , $\mathbf{F}_e \in \mathbb{R}^3$, and $\boldsymbol{\tau}_e \in \mathbb{R}^3$ are the interaction force and torque represented in \mathcal{F}_W and \mathcal{F}_B .

The control allocation design for the fully actuated flying platform is as follows: According to Fig. 4, we get [19]

$$\mathbf{R}_{P_i}^B(\alpha) = \mathbf{R}_z\left((i-1)\frac{\pi}{3}\right) \mathbf{R}_x((-1)^{i-1}\alpha), \quad i = 1, \dots, 6 \quad (4)$$

where $\alpha \in (0, \pi/2)$ represents the tilt angle of each rotor, and the factor of $(-1)^{i-1}$ is due to different tilts in opposite directions. $\mathbf{R}_x(\cdot)$ and $\mathbf{R}_z(\cdot)$ are the canonical rotation matrices about the x - and z -axes, respectively.

The position of O_{P_i} in \mathcal{F}_B can be expressed as follows [19]:

$$\mathbf{p}_{P_i}^B = \mathbf{R}_z\left((i-1)\frac{\pi}{3}\right) \begin{bmatrix} l & 0 & 0 \end{bmatrix}^T, \quad i = 1, \dots, 6 \quad (5)$$

where $l > 0$ represents the length from O_{P_i} to O_B .

According to (4) and (5), the thrust force and drag moment generated by the i th rotor are described as follows:

$$\mathbf{F}_{P_i}^B = c_f \varpi_i^2 \mathbf{R}_{P_i}^B(\alpha) \mathbf{e}_3, \quad i = 1, \dots, 6 \quad (6)$$

$$\boldsymbol{\tau}_{P_i}^B = (-1)^{i-1} c_r (c_f \varpi_i^2) \mathbf{R}_{P_i}^B(\alpha) \mathbf{e}_3, \quad i = 1, \dots, 6 \quad (7)$$

where c_f and c_r are constants that represent the thrust and torque coefficients of the propellers. ϖ_i represents the propeller speed. $c_f \varpi_i^2$ is the thrust generated by the i th propeller and $\mathbf{e}_3 = [0 \ 0 \ 1]^T$.

The force and torque exert on the CoM of the AM by the six rotors in \mathcal{F}_B can be expressed as follows:

$$\mathbf{F}_B(\alpha, \mathbf{u}_\varpi) = \sum_{i=1}^6 \mathbf{F}_{P_i}^B = \mathbf{F}_f(\alpha) \mathbf{u}_\varpi \quad (8)$$

$$\boldsymbol{\tau}(\alpha, \mathbf{u}_\varpi) = \sum_{i=1}^6 ((\mathbf{p}_{P_i}^B \times \mathbf{F}_{P_i}^B) + \boldsymbol{\tau}_{P_i}^B) = \mathbf{F}_\tau(\alpha) \mathbf{u}_\varpi \quad (9)$$

where $\mathbf{u}_\varpi = [c_f \varpi_1^2, \dots, c_f \varpi_6^2]^T$, $\mathbf{F}_f(\alpha) \in \mathbb{R}^{3 \times 6}$, and $\mathbf{F}_\tau(\alpha) \in \mathbb{R}^{3 \times 6}$ are constant matrices related to α .

According to (8) and (9), the control allocation matrix can be expressed as follows:

$$\mathbf{F}_\varpi(\alpha) = \begin{bmatrix} \mathbf{F}_f(\alpha) \\ \mathbf{F}_\tau(\alpha) \end{bmatrix} \in \mathbb{R}^{6 \times 6}. \quad (10)$$

When the six motors in Fig. 1 are coplanar, $\text{rank}(\mathbf{F}_\varpi(\alpha = 0)) = 4$, indicating that the AM is under actuated. When $\alpha \neq 0$, it can be derived that $\text{rank}(\mathbf{F}_\varpi(\alpha \neq 0)) = 6$, and the AM is fully actuated. The position control of the fully actuated AM does not depend on changes in attitude. Therefore, attaching the end effector to the AM enables stable aerial physical interaction.

B. Motion Control of the AM

The position control and attitude control of the AM have been decoupled. Without considering interaction forces, the feedback linearization method is employed to design controllers for the position and attitude loops of the AM. In this work, we directly control the velocity of the AM. The velocity controller of the AM is defined as follows:

$$\mathbf{R}_B^W \mathbf{F}_B = \frac{1}{m} \left(\mathbf{K}_{vp} \mathbf{e}_v + \mathbf{K}_{vi} \int_{t_0}^t \mathbf{e}_v dt + \mathbf{K}_{vd} \dot{\mathbf{e}}_v \right) + m g \mathbf{e}_3 \quad (11)$$

where $\mathbf{K}_{vp}, \mathbf{K}_{vi}, \mathbf{K}_{vd} \in \mathbb{R}^{3 \times 3}$ are the diagonal positive-definite gain matrices. $\mathbf{e}_v = \mathbf{v} - \mathbf{v}_d$ represents the velocity error w.r.t. \mathcal{F}_W , where \mathbf{v}_d is the desired velocity.

The attitude controller is expressed on $\text{SO}(3)$. $\mathbf{R}_d \in \mathbb{R}^{3 \times 3}$ represent the desired attitude and $\boldsymbol{\omega}_d = [\mathbf{R}_d^T \dot{\mathbf{R}}_d]_V$ is defined

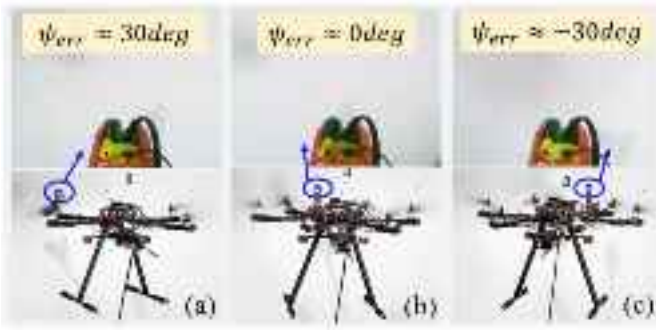


Fig. 5. AM and its camera perspective with different yaw errors. The top of (a)–(c) camera perspective, while the bottom depicts the AM with different yaw errors. When approaching the target surface, the camera views are similar under different yaw errors, making it difficult for the operator to control the AM's yaw based on these views.

as desired angular velocity, where $[\cdot]_{\vee}$ represents the inverse operator to convert $[\cdot]$ from $\text{so}(3)$ to \mathbb{R}^3 . Then, the attitude error $e_R \in \mathbb{R}^3$ can be defined as follows [12]:

$$e_R = \frac{1}{2} \left[R_d^T R_B^W - R_B^{W^T} R_d \right]_{\vee}. \quad (12)$$

The angular velocity tracking error $e_\omega \in \mathbb{R}^3$ is

$$e_\omega = \omega - R_B^{W^T} R_d \omega_d. \quad (13)$$

The attitude controller is defined as follows:

$$\tau = J^{-1} \left(K_{Rp} e_R + K_{Ri} \int_{t_0}^t e_R dt + K_{Rd} e_\omega \right) + \omega \times J \omega \quad (14)$$

where $K_{Rp}, K_{Ri}, K_{Rd} \in \mathbb{R}^{3 \times 3}$ are the diagonal positive-definite gain matrices.

IV. AERIAL CONTACT INSPECTION CONTROL SYSTEM DESIGN OF THE AM

In this section, we design control methods for the approach and contact phases of aerial contact inspection. For the approach phase, a yaw control assistance method has been presented, allowing the AM to autonomously adjust the yaw angle as it closes to the metal facility. For the contact phase, a force/velocity parallel controller is proposed to achieve the precise contact force control.

A. Yaw Control Assistance Method for the Approach Phase

As the AM closes to the target surface, the limited field of view of the camera makes it challenging for the operator to control the yaw of the AM through visual feedback. The AM and its camera perspective under different yaw errors are illustrated in Fig. 5.

As shown in Fig. 6, the calculation of the yaw error is as follows:

$$\psi_{err} = \arctan \left(\frac{D_l - D_r}{R} \right) \quad (15)$$

where ψ_{err} represents the yaw error, D_l and D_r represent the values of the two laser rangefinders, and R represents

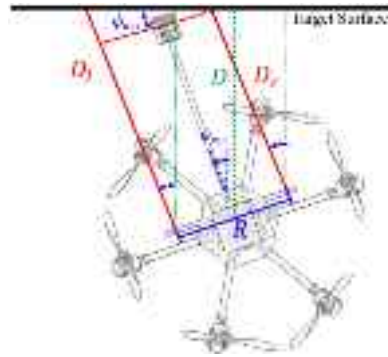


Fig. 6. Geometric relationship between the measurements of laser ranging sensors and the yaw error.

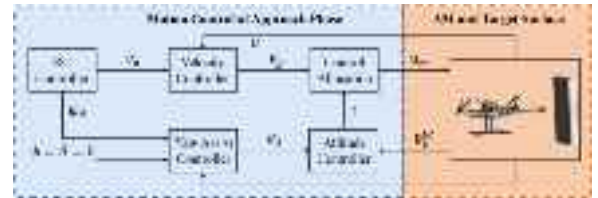


Fig. 7. Motion control framework of AM during the approach phase.

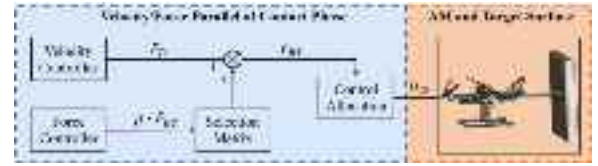


Fig. 8. Parallel force/velocity control framework during the interaction phase.

the installation distance between the rangefinders, which is measurable.

The distance D between the AM and the target surface is calculated as follows:

$$D = D_l \cos(\psi_{err}) + \frac{D_r \cos(\psi_{err})}{2}. \quad (16)$$

Based on distance D we can obtain the distance of the AM from the target surface, and when the distance is close, we can activate the yaw control assistance method. The motion control framework of the AM during the approach phase is illustrated in Fig. 7.

B. Parallel Force/Velocity Control for the Contact Phase

To achieve precise control of the interaction force during the contact phase of the AM, a force/velocity parallel control method is designed in this section. The control structure is depicted in Fig. 8.

The velocity control is shown in (11) with K_i is chosen as follows:

$$K_i = \begin{bmatrix} 0 & & \\ & K_{iy} & \\ & & K_{iz} \end{bmatrix}, \quad K_{iy} > 0, \quad K_{iz} > 0. \quad (17)$$

This means that a PD controller is used as velocity control in the interaction direction. When the AM interacts with the target surface, the PD velocity controller output generates interaction forces between the AM and the target surface due to the persistent velocity error. This interaction force control

strategy can also be referred to as damping control. However, for different interaction environments, it is challenging to select the desired velocity and PD parameters during the contact phase, making precise interaction force control difficult to achieve. Therefore, we parallel the force PI controller to the velocity controller to compensate for the interaction force error.

A selection matrix in this article is defined as follows:

$$\Lambda = \begin{bmatrix} 1 & & \\ & 0 & \\ & & 0 \end{bmatrix}. \quad (18)$$

The selection matrix determines the directions for which direct force control compensation is applied.

The design of the direct force PI controller is as follows:

$$\mathbf{F}_{Bf} = \Lambda \left(K_{fp} (\mathbf{F}_d - \mathbf{F}_e) + K_{fi} \int_{t_0}^t (\mathbf{F}_d - \mathbf{F}_e) dt \right) \quad (19)$$

where \mathbf{F}_d and \mathbf{F}_e represent the desired force and the interaction force measured by the force sensor with respect to \mathcal{F}_B , respectively.

Due to the noise of the force sensor causing undesirable switching behavior of the direct force controller, we designed a switching function as follows:

$$\rho(\mathbf{F}_d, \mathbf{F}_e, \mathbf{v}_d) = \begin{cases} 1, & \text{if } \mathbf{F}_e > 0 \text{ and } \Lambda \mathbf{F}_d^T \mathbf{v}_d > 0 \\ 0, & \text{if } \Lambda \mathbf{F}_d^T \mathbf{v}_d < 0. \end{cases} \quad (20)$$

The switching function in (20) indicates that when the measured value of the force sensor is greater than 0, indicating the AM end effector makes contact with the target surface, and when the desired force and the desired velocity is in the same direction, the direct force controller is activated. When the desired force is opposite to the desired velocity, the direct force PD controller is deactivated. This switching function avoids the undesirable switching behavior caused by force sensor noise and prevents the force controller from influencing the velocity controller in noncontact situations.

The parallel force/velocity controller is designed as follows:

$$\mathbf{F}_{B\parallel} = \mathbf{F}_B + \rho(\mathbf{F}_d, \mathbf{F}_e, \mathbf{v}_d) \mathbf{F}_{Bf}. \quad (21)$$

The force control acts as a compensator superimposed on the velocity PD controller. The integral action of the PI controller removes the steady state error of the interaction force, while the output of the velocity controller coincidentally corresponds to the feed-forward compensation of the direct force controller. The velocity controller is activated throughout the inspection process, which also avoids the possible unstable performance of the AM during the switching process between interaction control and motion control.

V. EXPERIMENTS AND RESULTS

A. Experimental Setup

The designed AM system, along with its hardware and software framework, is illustrated in Figs. 2 and 3. The NOKOV motion capture system provides the position and yaw data for the AM, while other attitude information is obtained from the Pixhawk 4's built-in IMU. The activation

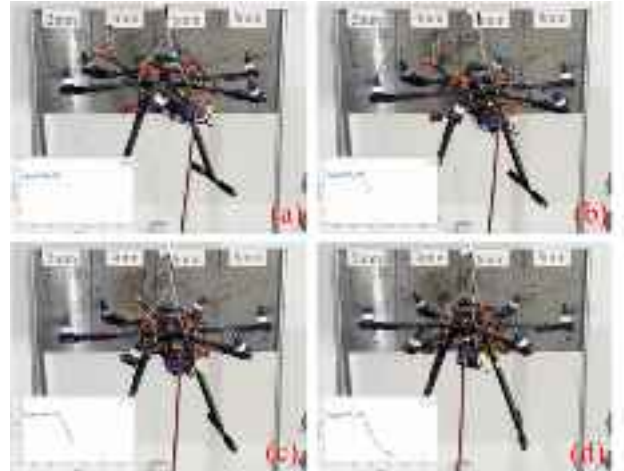


Fig. 9. Process of adjusting the yaw error of the AM. Subplots (a)–(d) show that the AM is autonomously adjusting the yaw error so that the x -axis of the \mathcal{F}_B is parallel to the direction normal to the target surface.

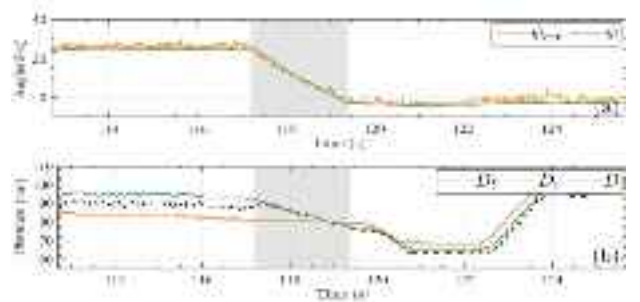


Fig. 10. Yaw control assistance method experimental results. The shaded area indicates that the AM is adjusting its yaw angle. (a) Yaw angle error of the AM and the AM yaw angle in \mathcal{F}_W . (b) Laser ranging sensor data and distance between two sensors center and target surface.

of the yaw control assistance and the parallel force/velocity controller is managed via different channels on the handheld radio transmitter.

In this section, we validate the proposed control methods and demonstrate the effectiveness of the AM system for aerial metal thickness measurement through practical experiments.

B. Experimental Results and Analysis of Control Methods

1) *Yaw Control Assistance Method Experiment*: The process of yaw adjustment of the AM is shown in Fig. 9. The normal direction of the target surface is parallel to the x -axis of \mathcal{F}_W . The AM operator activates the yaw adjustment assistance through a channel on the handheld radio transmitter, which adds the measured yaw error to the desired yaw as shown in Fig. 7. The experimental result is shown in Fig. 10. The shaded area in Fig. 9 represents the autonomous yaw adjustment of the AM. According to Fig. 10(a), it can be observed that the yaw control assistance method proposed in this article can calculate the yaw error between the AM and the normal of the target surface. Fig. 10(b) shows the data of the two distance sensors and the distance calculated by (16). Based on the distance D , we can obtain the distance from the end effector to the target surface.

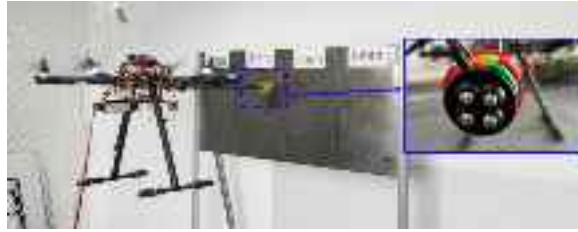


Fig. 11. AM is in point contact with the target surface.

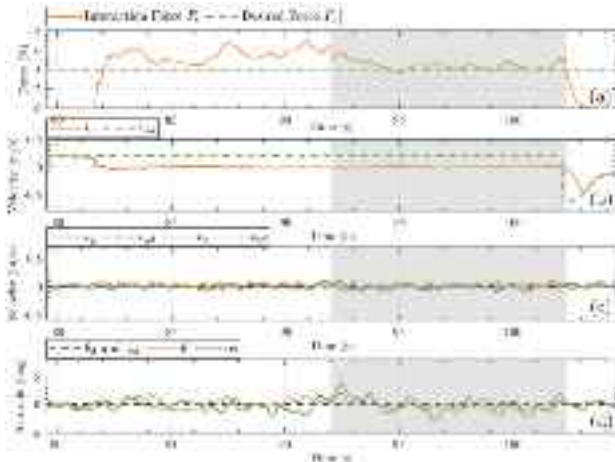


Fig. 12. Point contact experimental results. The shaded area indicates that the proposed parallel force/velocity controller is activated. (a) Interaction force between the AM and the target surface. (b) Velocity of the AM along the x -axis in \mathcal{F}_W . (c) Velocities of the AM along the y - and z -axes in \mathcal{F}_W . (d) Pitch and roll angles of AM.



Fig. 13. AM is in sliding contact with the target surface.

2) Point Contact Experiment: The AM makes point contact with the target surface as shown in Fig. 11. The results of the point contact experiment of the AM are shown in Fig. 12. We set the desired force to 4 N and the desired velocity during contact to 2 m/s. According to Fig. 12(a), when the force PI controller is not used, the interaction force is around 6 N, indicating that velocity error generates interaction force but the accuracy cannot be guaranteed. When using the proposed parallel force/velocity controller, the steady-state error of the interaction force significantly decreases, demonstrating that the proposed method can achieve more precise interaction force control. Fig. 12(b)-(d) shows the motion control data of the AM during the point contact process. According to Fig. 12(a), it can be observed that during the contact process, the pitch and roll of the AM are essentially 0°. This indicates that the designed fully actuated AM in this article is capable of generating controllable interaction forces without changing its attitude.

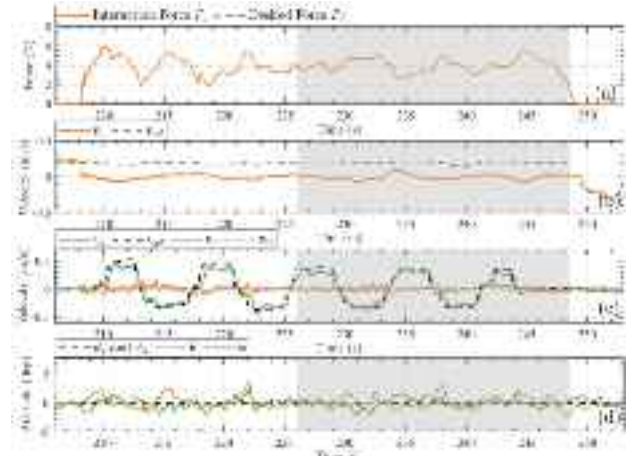


Fig. 14. Sliding contact experimental results. The shaded area indicates that the proposed parallel force/velocity controller is activated. (a) Interaction force between the AM and the target surface. (b) Velocity of the AM along the x -axis in \mathcal{F}_W . (c) Velocities of the AM along the y - and z -axes in \mathcal{F}_W . (d) Pitch and roll angles of the AM.



Fig. 15. AM is conducting steel plate thickness measurement.

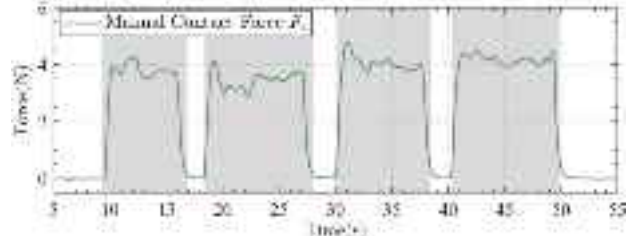


Fig. 16. Contact force during manual steel plate thickness measurement. The shaded area indicates the UT probe in contact with the steel plate.

3) Sliding Contact Experiment: In the sliding contact experiment, the AM applies an interaction force along the normal direction of the target surface while performing sliding motion on the surface, as shown in Fig. 13. The experimental results are shown in Fig. 14. According to Fig. 14(a), the proposed method improves force control accuracy. Fig. 14(b)-(d) shows the motion state of the AM, indicating that the proposed method can improve force control accuracy while ensuring good motion control performance when the AM performs large sliding movements.

C. Experimental Results and Analysis of AM-Based Steel Plate Thickness Measurement

We used a steel plate with varying thickness regions (2, 4, 6, and 8 mm) to simulate the metal structures intended for

TABLE III

THICKNESS MEASUREMENT OF STEEL PLATES IN DIFFERENT REGIONS BY MANUAL AND AM METHODS (UNITS: mm)

Region 1		Region 2		Region 3		Region 4	
Manual	AM	Manual	AM	Manual	AM	Manual	AM
2.32	2.38	4.20	4.26	6.20	6.20	8.42	8.38
2.30	2.30	4.20	4.24	6.22	6.18	8.38	8.38
2.32	2.30	4.26	4.24	6.24	6.20	8.40	8.42
2.36	2.32	4.22	4.28	6.20	6.22	8.40	8.12
2.40	2.36	4.22	4.40	6.00	6.16	8.36	8.36
2.32	2.36	4.24	4.38	6.20	6.20	8.40	8.36
Mean							
2.34	2.34	4.22	4.25	6.18	6.23	8.39	8.34
Std Dev							
0.037	0.034	0.023	0.072	0.088	0.021	0.021	0.108
ExpUnc							
0.0294	0.0276	0.0187	0.0573	0.0704	0.0165	0.0165	0.0876

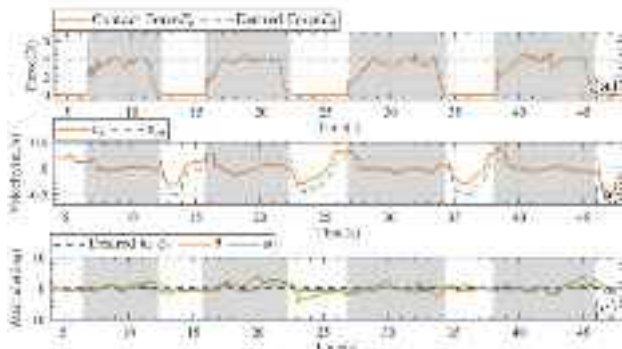


Fig. 17. Contact force and motion state of the AM during steel plate thickness measurement. The shaded area indicates the UT probe in contact with the steel plate. (a) Interaction force between AM and target surface. (b) Velocity of the AM along the x -axis in F_w . (c) Pitch and roll angles of the AM.

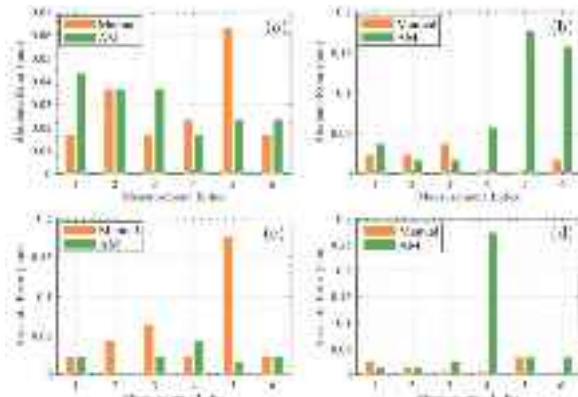


Fig. 18. Absolute error comparison between manual and AM measurements across different thickness regions. Subplots (a)-(d) are the absolute error comparison of regions 1–4 with different thicknesses.

inspection. The operator remotely controlled the AM to contact each thickness region, as shown in Fig. 15. Upon contact between the end effector and the steel plate, the inspection personnel retrieved the thickness data on the host computer, with the UT gauge sending measurements every second. The AM performed six measurements at each thickness region. For comparison, a human inspector performed six measurements in each area where the AM conducted its tests, with couplant residue remaining at the AM measurement locations. Given

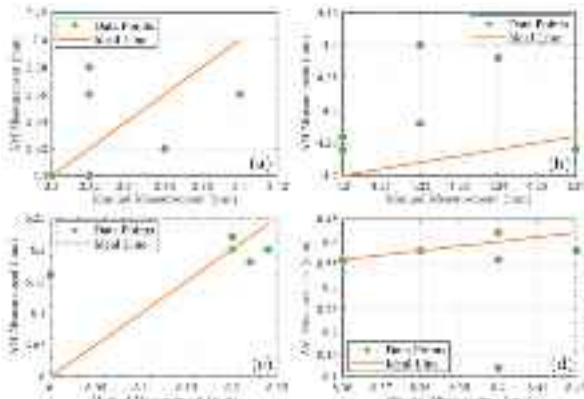


Fig. 19. Consistency comparison between AM and manual measurements across different thickness regions. Subplots (a)-(d) are the absolute error comparison of regions 1–4 with different thicknesses.

the manufacturing tolerances of the steel plate, the average of the manual measurements was considered the true thickness. The results, including the data from both AM and manual measurements, as well as the mean, standard deviation, and uncertainty, are presented in Table III.

The contact force during manual steel plate thickness measurements is approximately 4 N, as shown in Fig. 16. Consequently, the contact force for AM-based inspections was also set to 4 N. Fig. 17 illustrates the AM's contact force and motion state during the inspection process, where the AM maintains stability while transitioning between free flight and contact inspection, with the contact force consistently around 4 N.

To visualize the deviation of both manual and AM measurements from the true value, we generated an error bar chart displaying the absolute error across the four thickness regions, as shown in Fig. 18. In regions 1 and 3, the AM measurements demonstrated performance similar to manual measurements, with minimal deviation from the true value. However, Fig. 18(b) shows a significant error in the AM system at measurement indices 5 and 6. In the fourth measurement of region 4, as seen in Fig. 18(d), a larger measurement error occurs. This discrepancy likely results from a slight wobble in the AM's attitude, potentially creating a small gap between the UT probe and the steel plate, which increases the measurement error, as indicated by the attitude of the AM during inspection in Fig. 17(c).

To assess the consistency between the manual and AM measurement methods, we generated scatter plots, as shown in Fig. 19. Each plot includes data points alongside an ideal line representing perfect correlation ($y = x$). In regions 1 and 3, as shown in Fig. 19(a) and (b), the data points closely follow the ideal line, indicating good agreement between AM and manual measurements. In the higher thickness regions Fig. 19(c) and (d), some deviations from the ideal line are observed, but the overall trend shows that AM measurements are still consistent with manual results.

According to Table III, we calculated the standard deviation and expanded uncertainty of both manual and AM measurements across different thickness regions. The expanded uncertainty, using a 95% confidence interval (coverage factor

$k = 1.96$, provides a measure of the confidence in the measurements, indicating the range within which the true value is likely to lie. In regions 1 and 3, the standard deviation and expanded uncertainty of AM measurements are equal to or lower than those of manual measurements, indicating that the AM system can achieve reliable and accurate results. This consistency suggests that the AM's performance in these regions is comparable with manual methods, with uncertainty analysis supporting the system's precision. However, in regions 2 and 4, the AM system exhibits higher standard deviation and expanded uncertainty, particularly in region 4. This increase is attributed to the larger deviations in certain measurements, likely caused by AM attitude instability during the inspection process, as shown in Fig. 17(c). Despite these occasional higher uncertainties, the AM system remains within a reasonable error range, demonstrating its robustness and potential for thickness measurements of aerial metal structures. The expanded uncertainty analysis further validates the AM system's effectiveness. We believe it can be reliably used in practical applications with appropriate measures to manage outliers and ensure AM motion stability.

VI. CONCLUSION AND FUTURE WORKS

This article presents a fully actuated AM system and its control method for thickness measurement of aerial metal facilities. Due to the fully actuated advantage of the flying platform, the end effector is fixedly attached to the aerial platform and does not require additional DoF to apply interaction forces to the target surface. Designed end effector enables thickness measurement of metal facilities and automatic extrusion of coupling agent. The yaw control assistance method enables the AM to make contact with the target surface at the desired attitude, ensuring the safety of aerial contact inspections. The proposed parallel force–velocity controller can achieve accurate force control in the contact phase. The comparison between AM-based steel plate thickness measurements and manual measurements reveals that, despite a few data points with significant errors in the AM-based measurements, the overall results are similar to those obtained manually. The AM system designed in this study applies to the thickness measurement of aerial metal structures. The experimental results indicate that the contact stability of the AM system can influence the measurement outcomes. In future work, we will focus on achieving stable contact control for AMs in the presence of external disturbances, particularly in controlling the contact force.

REFERENCES

- [1] T. Czimmermann et al., "An autonomous robotic platform for manipulation and inspection of metallic surfaces in industry 4.0," *IEEE Trans. Autom. Sci. Eng.*, vol. 19, no. 3, pp. 1691–1706, Jul. 2022.
- [2] Z. Wang, S. Liu, G. Chen, and W. Dong, "Robust visual positioning of the UAV for the under bridge inspection with a ground guided vehicle," *IEEE Trans. Instrum. Meas.*, vol. 71, pp. 1–10, 2022.
- [3] Y. Liu, J. Dong, Y. Li, X. Gong, and J. Wang, "A UAV-based aircraft surface defect inspection system via external constraints and deep learning," *IEEE Trans. Instrum. Meas.*, vol. 71, pp. 1–15, 2022.
- [4] C. Xu, Q. Li, Q. Zhou, S. Zhang, D. Yu, and Y. Ma, "Power line-guided automatic electric transmission line inspection system," *IEEE Trans. Instrum. Meas.*, vol. 71, pp. 1–18, 2022.
- [5] T. Ye, W. Qin, Z. Zhao, X. Gao, X. Deng, and Y. Ouyang, "Real-time object detection network in UAV-vision based on CNN and transformer," *IEEE Trans. Instrum. Meas.*, vol. 72, pp. 1–13, 2023.
- [6] J. Huang, Y. Shen, J. Wang, and V. Ferreira, "Automatic pylon extraction using color-aided classification from UAV LiDAR point cloud data," *IEEE Trans. Instrum. Meas.*, vol. 72, pp. 1–11, 2023.
- [7] Z. Li, H. Wu, Q. Wang, W. Wang, S. Suzuki, and A. Namiki, "Small UAV urban overhead transmission line autonomous correction inspection system based on radar and RGB camera," *IEEE Sensors J.*, vol. 24, no. 5, pp. 5593–5608, Mar. 2024.
- [8] T. Zhang, Z. Yang, Z. Xu, and J. Li, "Wheat yellow rust severity detection by efficient DF-UNet and UAV multispectral imagery," *IEEE Sensors J.*, vol. 22, no. 9, pp. 9057–9068, May 2022.
- [9] A. Ollero, M. Tognon, A. Suarez, D. Lee, and A. Franchi, "Past, present, and future of aerial robotic manipulators," *IEEE Trans. Robot.*, vol. 38, no. 1, pp. 626–645, Feb. 2022.
- [10] V. Ghadiok, J. Goldin, and W. Ren, "Autonomous indoor aerial gripping using a quadrotor," in *Proc. IEEE/RSJ Int. Conf. Intell. Robots Syst.*, Sep. 2011, pp. 4645–4651.
- [11] G. Garimella and M. Kobilarov, "Towards model-predictive control for aerial pick-and-place," in *Proc. IEEE Int. Conf. Robot. Autom. (ICRA)*, May 2015, pp. 4692–4697.
- [12] S. Hao et al., "Vision-based autonomous detecting and grasping framework for the fully-actuated aerial manipulator," in *Proc. IEEE Int. Conf. Robot. Biomimetics (ROBIO)*, Dec. 2023, pp. 1–6.
- [13] B. Stephens, H.-N. Nguyen, S. Hamaza, and M. Kovac, "An integrated framework for autonomous sensor placement with aerial robots," *IEEE/ASME Trans. Mechatronics*, vol. 28, no. 1, pp. 38–49, Feb. 2023.
- [14] Y. Chen et al., "Adaptive stiffness visual servoing for unmanned aerial manipulators with prescribed performance," *IEEE Trans. Ind. Electron.*, vol. 71, no. 9, pp. 11028–11038, Sep. 2024.
- [15] Y. Wu et al., "Dynamic image-based impedance control of aerial manipulator for sliding inspection," *IEEE/ASME Trans. Mechatronics*, vol. 29, no. 6, pp. 11028–11038, Dec. 2024.
- [16] M. Ryll et al., "6D interaction control with aerial robots: The flying end-effector paradigm," *Int. J. Robot. Res.*, vol. 38, no. 9, pp. 1045–1062, Aug. 2019.
- [17] K. Bodie et al., "Active interaction force control for contact-based inspection with a fully actuated aerial vehicle," *IEEE Trans. Robot.*, vol. 37, no. 3, pp. 709–722, Jun. 2021.
- [18] W. Zhang, L. Ott, M. Tognon, and R. Siegwart, "Learning variable impedance control for aerial sliding on uneven heterogeneous surfaces by proprioceptive and tactile sensing," *IEEE Robot. Autom. Lett.*, vol. 7, no. 4, pp. 11275–11282, Oct. 2022.
- [19] S. Hao, G. Song, J. Mao, Y. Gu, and A. Song, "A fully actuated aerial manipulator system for industrial contact inspection applications," *Ind. Robot. Int. J. Robot. Res. Appl.*, vol. 50, no. 3, pp. 421–431, Apr. 2023.
- [20] T. Kominami, Z. Liang, R. R. Martinez, H. Paul, and K. Shimonomura, "Physical contact with wall using a multirotor UAV equipped with add-on thruster for inspection work," in *Proc. IEEE/RSJ Int. Conf. Intell. Robots Syst. (IROS)*, Oct. 2023, pp. 6955–6961.
- [21] A. C. Fauli et al., "Assisted flight control for aerial contact UAVs in industrial environments," in *Proc. Aerial Robotic Syst. Physically Interacting Environ.*, Apr. 2021, pp. 1–4.
- [22] R. Rashad et al., "Energy aware impedance control of a flying end-effector in the port-Hamiltonian framework," *IEEE Trans. Robot.*, vol. 38, no. 6, pp. 3936–3955, Dec. 2022.
- [23] M. Xu, A. Hu, and H. Wang, "Image-based visual impedance force control for contact aerial manipulation," *IEEE Trans. Autom. Sci. Eng.*, vol. 20, no. 1, pp. 518–527, Jan. 2023.
- [24] G. Nava, Q. Sablé, M. Tognon, D. Pucci, and A. Franchi, "Direct force feedback control and online multi-task optimization for aerial manipulators," *IEEE Robot. Autom. Lett.*, vol. 5, no. 2, pp. 331–338, Apr. 2020.
- [25] M. Schumacher, J. Wojtusch, P. Beckerle, and O. von Stryk, "An introductory review of active compliant control," *Robot. Auto. Syst.*, vol. 119, pp. 185–200, Sep. 2019.
- [26] C. Schindlbeck and S. Haddadin, "Unified passivity-based Cartesian force/impedance control for rigid and flexible joint robots via task-energy tanks," in *Proc. IEEE Int. Conf. Robot. Autom. (ICRA)*, May 2015, pp. 440–447.
- [27] R. Rashad, J. B. C. Engelen, and S. Stramigioli, "Energy tank-based wrench/impedance control of a fully-actuated hexarotor: A geometric port-Hamiltonian approach," in *Proc. Int. Conf. Robot. Autom. (ICRA)*, May 2019, pp. 6418–6424.



Shuang Hao (Member, IEEE) received the M.S. degree from Nanchang University, Nanchang, China, in 2020. He is currently pursuing the Ph.D. degree with Southeast University, Nanjing, China.

His research interests include aerial manipulators, bilateral teleoperation systems, and nonlinear system control.



Guangming Song (Senior Member, IEEE) received the Ph.D. degree in control science and engineering from the University of Science and Technology of China, Hefei, China, in 2004.

From 2004 to 2006, he was a Research Fellow at the Robotic Sensor and Control Laboratory, Southeast University, Nanjing, China. Since 2006, he has been with the School of Instrument Science and Engineering, Southeast University, where he is currently a Professor. His current research interests include distributed robots, aerial manipulators, and bioinspired legged robots.



Juzheng Mao (Graduate Student Member, IEEE) received the M.S. degree in power engineering from Beijing Institute of Technology, Beijing, China, in 2016. He is currently pursuing the Ph.D. degree in instrument science and technology with Southeast University, Nanjing, China.

His research interests include multirobot systems and underwater manipulators.



Aiguo Song (Senior Member, IEEE) received the B.S. degree in automatic control and the M.S. degree in measurement and control from Nanjing University of Aeronautics and Astronautics, Nanjing, China, in 1990 and 1993, respectively, and the Ph.D. degree in measurement and control from Southeast University, Nanjing, in 1996.

He is currently a Professor and a Doctoral Supervisor with the School of Instrument Science and Engineering, Southeast University, and the Director of the Robot Sensing and Control Technology Laboratory. His research interests include haptic displays, robot tactile sensors, rehabilitation engineering, and robotic teleoperation technology.



Junyi Zhang received the B.E. degree in measurement and control technology and instrument from Hefei University of Technology, Hefei, China, in 2019, and the M.S. degree in electronic and information engineering from Tianjin University, Tianjin, China, in 2023. He is currently pursuing the Ph.D. degree in instrument science and technology with Southeast University, Nanjing, China.

His research interests include aerial manipulators, signal processing, and nonlinear system control.



Peter Xiaoping Liu (Fellow, IEEE) received the B.Sc. degree in mechanical engineering and the M.Sc. degree in instrumentation and control engineering from Northern Jiaotong University, Beijing, China, in 1992 and 1995, respectively, and the Ph.D. degree in electrical and computer engineering from the University of Alberta, Edmonton, AB, Canada, in 2002.

Since July 2002, he has been with the Department of Systems and Computer Engineering, Carleton University, Ottawa, ON, Canada, where he is currently a Professor. His research interests include interactive networked systems and teleoperation, haptics, surgical simulation, control, and intelligent systems.

Dr. Liu is a Licensed Member of the Professional Engineers of Ontario (P.Eng.) and a fellow of the Engineering Institute of Canada (FEIC), the Canadian Academy of Engineering (FCAE), and the Institute of Electrical and Electronics Engineers (IEEE). He was an Associate Editor for several journals, including IEEE/ASME TRANSACTIONS ON MECHATRONICS, IEEE TRANSACTIONS ON CYBERNETICS, IEEE TRANSACTIONS ON AUTOMATION SCIENCE AND ENGINEERING, IEEE/CAA JOURNAL OF AUTOMATICA SINICA, and IEEE TRANSACTIONS ON INSTRUMENTATION AND MEASUREMENT.



Xiangyang Zhao received the B.E. degree in automation from Anhui University of Science and Technology, Huainan, China, in 2019. He is currently pursuing the M.S. degree in instrument science and technology with Southeast University, Nanjing, China.

His research interests include aerial manipulators.